Influence of particle velocity when propelled using N2 or N2-He mixed gas on the properties of cold-sprayed Ti6Al4V coatings

Tan, Adrian Wei-Yee; Lek, Jun Yan; Boothroyd, Chris Brian; Sun, Wen; Bhowmik, Ayan; Marinescu, Iulian; Song, Xu; Zhai, Wei; Li, Feng; Dong, Zhili; Liu, Erjia

2018

Tan, A. W.-Y., Lek, J. Y., Sun, W., Bhowmik, A., Marinescu, I., Song, X., . . . Liu, E. (2018). Influence of particle velocity when propelled using N2 or N2-He mixed gas on the properties of cold-sprayed Ti6Al4V coatings. Coatings, 8(9), 327-. doi:10.3390/coatings8090327

https://hdl.handle.net/10356/103681

https://doi.org/10.3390/coatings8090327

coatings

MDPI

Article

Influence of Particle Velocity When Propelled Using N_2 or N_2-He Mixed Gas on the Properties of Cold-Sprayed Ti6Al4V Coatings

Adrian Wei-Yee Tan [1,2], Jun Yan Lek [1,3], Wen Sun [1,2], Ayan Bhowmik [1,2], Iulian Marinescu [1,5], Xu Song [4], Wei Zhai [4], Feng Li [1,5], Zhili Dong [6], Chris B. Boothroyd [3,6] and Erjia Liu [1,2,*]

1 Rolls-Royce@NTU Corporate Lab, Nanyang Technological University, 50 Nanyang Avenue, Singapore 639798, Singapore; adriantan@ntu.edu.sg (A.W.-Y.T.); jylek@ntu.edu.sg (J.Y.L.); SUNW0013@e.ntu.edu.sg (W.S.); abhowmik@ntu.edu.sg (A.B.); Iulian.Marinescu2@Rolls-Royce.com (I.M.); Feng.Li2@Rolls-Royce.com (F.L.)
2 School of Mechanical & Aerospace Engineering, Nanyang Technological University, 50 Nanyang Avenue, Singapore 639798, Singapore
3 Facility for Analysis, Characterisation, Testing and Simulation (FACTS), Nanyang Technological University, 50 Nanyang Avenue, Singapore 639798, Singapore; ChrisBoothroyd@cantab.net
4 Singapore Institute of Manufacturing Technology (SIMTech), 73 Nanyang Drive, Singapore 637662, Singapore; xsong@simtech.a-star.edu.sg (X.S.); zhaiw@simtech.a-star.edu.sg (W.Z.)
5 Advanced Technology Centre, Rolls-Royce Singapore Pte Ltd., 1 Seletar Aerospace Crescent, Singapore 797575, Singapore
6 School of Materials Science and Engineering, Nanyang Technological University, 50 Nanyang Avenue, Singapore 639798, Singapore; ZLDong@ntu.edu.sg
* Correspondence: mejliu@ntu.edu.sg; Tel.: +65-6790-5504

Received: 12 July 2018; Accepted: 7 September 2018; Published: 18 September 2018

Abstract: Cold-spraying is a relatively new low-temperature coating technology which produces coatings by the deposition of metallic micro-particles at supersonic speed onto target substrate surfaces. This technology has the potential to enhance or restore damaged parts made of light metal alloys, such as Ti6Al4V (Ti64). Particle deposition velocity is one of the most crucial parameters for achieving high-quality coatings because it is the main driving force for particle bonding and coating formation. In this work, studies were conducted on the evolution of the properties of cold-sprayed Ti64 coatings deposited on Ti64 substrates with particle velocities ranging from 730 to 855 m/s using pure N_2 and N_2-He mixture as the propellant gases. It was observed that the increase in particle velocity significantly reduced the porosity level from about 11 to 1.6% due to greater densification. The coatings' hardness was also improved with increased particle velocity due to the intensified grain refinement within the particles. Interestingly, despite the significant differences in the coating porosities, all the coatings deposited within the velocity range (below and above critical velocity) achieved a high adhesion strength exceeding 60 MPa. The fractography also showed changes in the degree of dimple fractures on the particles across the deposition velocities. Finite element modelling was carried out to understand the deformation behaviour of the impacting particles and the evolutions of strain and temperature in the formed coatings during the spraying process. This work also showed that the N_2-He gas mixture was a cost-effective propellant gas (up to 3-times cheaper than pure He) to deliver the high-quality Ti64 coatings.

Keywords: high-pressure cold spray; Ti6Al4V powder/coating/substrate; particle velocity; N_2-He gas mixture; adhesion strength; finite element modelling

1. Introduction

Titanium (Ti) alloys, such as Ti6Al4V (Ti64), possess superb properties like low density, high specific strength and good corrosion resistance, and are ideal to be used in aerospace, chemical, and biomedical applications [1]. As these Ti64 components suffer from wear and tear over the service period, it will be more cost-effective to repair them and restore their functionality instead of scraping or refabrication. Conventional repair methods such as welding and direct laser deposition may not be most suitable for the repair work as they involve high processing temperatures. These techniques often lead to heat-affected zones and high thermal stresses which lead to distortion, undesired phase change or transformation, which may create mechanical weak points for failure [2–4]. Cold spraying (CS) is a low-temperature additive manufacturing process, which could be an alternative technique to repair these components.

CS is a process whereby particles (1 to 100 μm) are accelerated to speeds up to 1000 m/s or more by supersonic gas flow and then impact on the target substrate surface to form a dense coating. The particles remain in a solid-state condition throughout the deposition process [5]. The detailed working principle of the CS process has been widely reported in the literature [6–14]. The particle deposition velocity (or particle velocity) has the most significant impact on the bonding of particles [15–17]. At the minimum deposition velocity or critical velocity, the particles would have just enough kinetic energy to activate adiabatic shear instabilities on the impacted surface, i.e., the particles and substrate, to form the bonding. The adiabatic shear instabilities would allow the particle contact interfaces to thermally soften, severely deform and create material jetting, as well as forming refined grains for metallurgical bonding and mechanical interlocking [12,13,18–20]. Hence, the impact velocity would affect the coating qualities such as adhesion, cohesive strength, deposition efficiency, hardness, etc. [21]. Other factors that would influence the coating quality are substrate surface condition (temperature, roughness, hardness [21–24]), particle type and size [25], impact angle [26], etc. The optimum particle velocity differs for different types of material due to their different yield strengths and melting points [27,28]. To date, there have been many studies of the influence of particle velocity for different pure metals such as aluminium, copper, and titanium as well as steels [29–38].

Several studies have been reported on understanding of the influence of particle velocity on the properties of cold-sprayed Ti64 coatings, as there is a need for the repair or enhancement of Ti64 components. The particle velocity of Ti64 can be controlled by the type of carrier gas (e.g., air, nitrogen (N_2) and helium (He)), gas pressure (20 to 50 bar), gas temperature (500 to 1000 °C), etc. A lighter gas, He or a mixture of N_2 and He, with high gas pressure and a preheated temperature would generate a faster gas stream and provide a higher drag force onto each particle (for acceleration), which results in a more significant particle deformation upon impact and improves coating quality [39–43].

Goldbaum et al. [44] studied the effect of particle velocity on deposited splats (single particle impacts) for a range of velocities. The flattening of Ti64 particles was increased by 50% when the particles were accelerated from around 600 to 800 m/s. However, the flattening of the splats seemed to reach a plateau when deposited at 800 to 1000 m/s. Although the particles were deposited at 800 m/s and above on the substrate (25 °C), the splat–substrate interface appeared to have microcracks and not be well-bonded, which resulted in a low splat adhesion strength of about 100 MPa, while the splat adhesion strength could be improved up to about 250 MPa when the coatings were deposited on preheated substrate surfaces (400 °C). Vidaller et al. [45] showed that Ti64 splats had better adhesion (on Ti64 grade 2 substrates) and more deformation when deposited using pure N_2 gas under higher pressure and temperature (e.g., 50 bar, 1000 °C).

Table 1 shows the previous studies on the CS deposition of full Ti64 coatings. The coating qualities (such as porosity level and hardness) can be easily improved by using higher gas pressure and temperature and He gas. However, as He gas is much more expensive than N_2 gas, it is not economical to be used in industry. In addition, the gas preheating threshold, at around 1100 °C, would limit the highest attainable particle velocity. If a more powerful gas heater is used (assuming a preheating temperature of 1200 to 1600 °C), there is a possibility of powder degradation (phase changes) in flight.

There are fewer studies on the cold-sprayed deposition of Ti64 coatings on Ti64 substrates across a range of velocities and using an N_2-He (N_2 gas based) gas mixture as a propellant gas, as compared to other materials [39–41]. The effects of particle velocity on the coating properties were studied in this work, which demonstrated that the usage of the N_2-He gas mixture as a propellant gas could improve the overall coating quality, while keeping other process parameters constant. The porosity level, microstructure, mechanical properties, and fracture behaviour of the coatings were systematically investigated. Finite element modelling was also used to understand the particle impact phenomena at different particle velocities.

Table 1. Review of CS deposited Ti64 coatings on Ti64 substrates.

Author (et al.)	Ref.	Gas Type (*P*, *T*)	Porosity (%)	Microhardness (HV)	Adhesion Strength (MPa)
Bhattiprolu	[25]	He (41, 425) He (41, 500)	0.9 1.16	415 400	>65 50 ± 12
Vo	[46]	N_2 (40, 800) He (40 ,350)	12 1	350 357	– –
Luo	[47]	N_2 (28, 550) He (28, 550)	15.7 2.7	210 363	– –
Birt	[48]	N_2 (38.5, 760) N_2-73 vol.% He (36, 790)	11.3 2.1	214.1 * 517 *	– –
Li	[49]	Air (28, 520)	22.3	–	–
Aydin	[50]	N_2 (40, 800)	6.7	385	–
Garrido	[51]	N_2 (40, 800) N_2 (50, 1000)	18.1 3.83	328.3 361	– –
Perton	[22]	N_2 (40, 800)	7.5	860	>80

P, Pressure (bar); *T*, Temperature (°C); * measured with nanoindentation test.

2. Experimental Details

2.1. Materials

Ti64 (Grade 5) discs (Titan Engineering, Singapore) with a 25 mm diameter and 5 mm thickness were used as substrates. The substrates were polished to a mirror-like surface (with P1200 grit paper followed by fine polishing with Struers (Cleveland, OH, USA) DiaPro (9 µm diamond paste) and OP-S (0.04 µm colloidal silica) suspension) and degreased sequentially before cold-spray deposition. As shown in Figure 1a, plasma-atomized spherical Ti64 ELI (Grade 23) powder with an average size ranging from 15 to 45 µm was used as the feedstock powder. The backscattered electron image (BEI) of an unetched powder cross-section is shown in Figure 1b and consists of martensitic α′-Ti lathes due to its quenching process [48]. The particle size distributions measured by laser diffraction (ASTM B822-10) [52] for D10, D50 and D90 were 19, 33 and 45 µm, respectively.

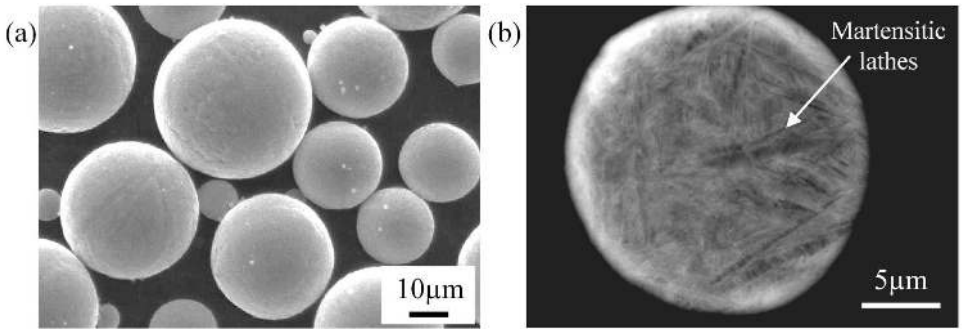

Figure 1. SEM images of (**a**) Ti64 powder (grade 23) and (**b**) cross-section of a Ti64 particle under back-scattered mode.

2.2. Cold-Spray Process

The Ti64 coatings were deposited using an Impact Spray System 5/11 (Impact Innovations, Rattenkirchen, Germany) with the setup shown in Figure 2a [53]. A SiC spray nozzle of 6 mm diameter with an expansion ratio of 5.6, throat diameter of 2.54 mm and a divergent section length of 160 mm was used in the CS deposition. The stand-off distance between the nozzle and substrate was 30 mm. The sample stage was moved from left-to-right horizontally with a constant velocity of 500 mm/s (Figure 2b) followed by 1 mm vertical raster step after each traverse movement to form a coated layer until the coating thickness deposited was around 1.5 to 2 mm for each sample (Figure 2c). The nozzle was water-cooled. The deposition parameters are shown in Table 2. The particle velocity was measured using a Cold Spray Meter (Tecnar, Saint-Bruno-de-Montarville, QC, Canada). The numerical calculations of particle velocity and temperature were conducted using the Kinetic Spray Solutions (KSS) software package (Kinetic Spray Solutions, Buchholz, Germany) [54]. Usage of the KSS software has also been reported elsewhere [30,45,55]. More details of calculations for the N_2-He gas mixture can be found in [39].

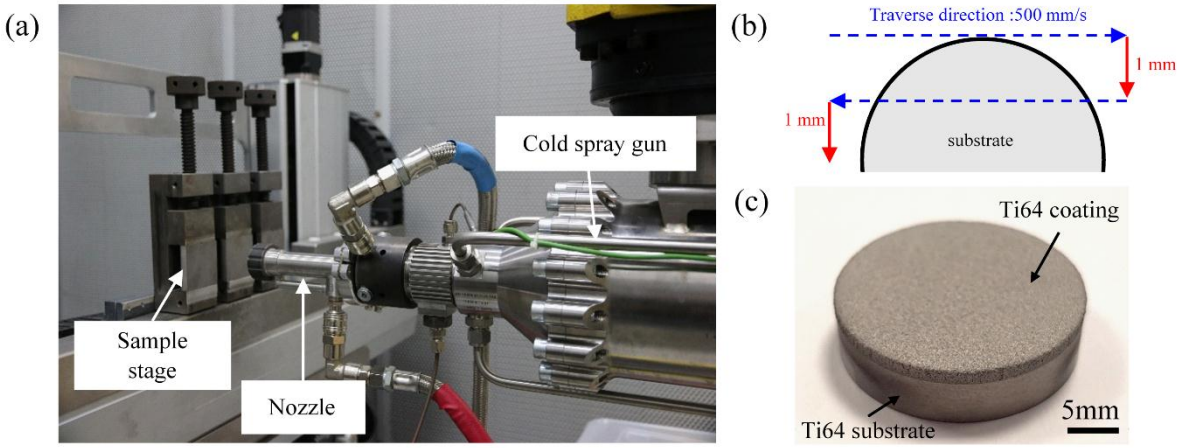

Figure 2. (**a**) Cold-spray setup (shown in previous work [53]); (**b**) illustration of nozzle's scanning path and (**c**) photograph of a cold-sprayed Ti64 sample.

Table 2. Cold-spray deposition parameters.

Working Gas (vol.%)		Gas Pressure (MPa)	Gas Temperature (°C)	Measured Particle Velocity (m/s)
Nitrogen	Helium			
100	–	4.5	800	~730
100	–		900	~760
100	–		1000	~800
90	10		1000	~827
80	20		1000	~855

2.3. Microstructural and Mechanical Characterisation

For the cross-section analysis, each cold-sprayed sample was cut into halves with the coating dimensions of 25 mm (length) × 6.5–7 mm (thickness). The cut samples were mounted with Polyfast, ground with SiC #320, followed by chemical–mechanical polishing (CMP) with a DiaPro solution containing 9 µm diamond particles and then an OP-S suspension solution containing 0.04 µm colloidal silica particles (Struers, Ballerup, Denmark). The polished samples were etched for the microstructural evaluation using Kroll's reagent by immersion method for 10 to 15 s.

Microstructures and porosities of the samples were observed under optical microscope (OM, Axioskop 2 MAT, Carl Zeiss, Oberkochen, Germany) and/or scanning electron microscope (SEM JSM-5600LV and FESEM 7600f, JEOL, Peabody, MA, USA) operated at 15 to 30 kV. For the porosity

measurement, at least 10 continuous cross-section images (optical, ×100 magnification) were taken from the coating top, middle and near-interface regions. These images were stitched (per location) and processed using the open source software ImageJ (NIH, Bethesda, MD, USA) [48].

The microhardnesses of the cross-sections of the coated Ti64 samples were evaluated using a Vickers microindenter (FM-300e, Future-Tech, Kanagawa, Japan), with 300 g load and 15 s dwell time. A total of 10 indentation measurements were randomly conducted on the cross-section of each sample and an average microhardness value was calculated.

Adhesion strength testing was conducted on each coated sample following the ASTM C633 standard [56]. The detailed assembly steps for the testing samples were reported in [53]. An assembled sample was tested using a tensile tester (Instron 5569, High Wycombe, UK) with a load cell of 50 kN in tensile mode with an extension rate of 0.8 mm/min until the sample failed.

2.4. Finite Element Modelling

ABAQUS/Explicit finite element analysis software was used for the 3D modelling of the Ti64 particle–Ti64 substrate impact process. Figure 3 shows an isometric view to better illustrate the meshes and the exact positions of the particle and substrate. The particle temperatures were estimated from the KSS software [54]. The particle impact velocities selected were the two extreme ends of the study, i.e., 730 and 855 m/s, while the particle temperatures were set to be 754 and 865 K, respectively, obtained from the KSS software [54]. The substrate temperature was set at 573 K as a result of preheating [53]. The particle size was fixed at 30 µm for the simulations and the substrate had a diameter of 120 µm (4-times larger than the particle size) and a height of 60 µm. The mesh size of the substrate ranged from 0.3 µm at the impact center to 1 µm at the edge wall, while the particle mesh size was set as 0.6 µm (1/50 of the particle diameter d_p) and gradually decreased to 0.3 µm (1/100 of the particle diameter d_p) towards the impacted region. The monitored elements are A, B and C as illustrated in Figure 3b.

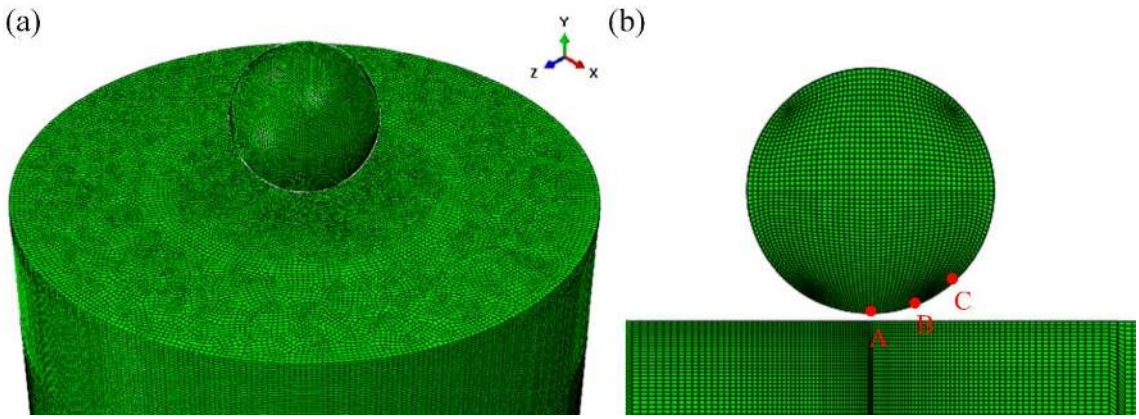

Figure 3. (**a**) Finite element mesh of a full 3D model for a single particle's normal impact onto the substrate and (**b**) a zoom-in view of the particle–substrate interface with the respective locations of elements A, B and C.

The Johnson-Cook plasticity model was used to determine the effects of strain hardening, strain rate hardening and thermal softening on the equivalent plastic deformation resistance. This model has been widely used to simulate the jetting phenomenon of particle impact during cold spraying [12,14,18,27,34,57–68], despite its limitation at very high strain rates [57,69,70]. The equivalent plastic stress of the material is given as follows:

$$\overline{\sigma} = [\mathrm{A} + \mathrm{B}(\overline{\varepsilon}^{P})^{\mathrm{n}}]\left[1 + \mathrm{C}\ln\left(\frac{\dot{\overline{\varepsilon}}^{p}}{\dot{\overline{\varepsilon}}^{p}{}_{0}}\right)\right]\left[1 - \left(\frac{T - T_{ref}}{T_m - T_{ref}}\right)^{\mathrm{m}}\right] \quad (1)$$

where $\overline{\sigma}$ is the equivalent plastic stress or flow stress (MPa), $\overline{\varepsilon}^{P}$ is the equivalent plastic strain (s^{-1}), $\dot{\overline{\varepsilon}}^{p}$ is the equivalent plastic strain rate (s^{-1}), $\dot{\overline{\varepsilon}}^{p}{}_{0}$ is the reference equivalent plastic stain rate (s^{-1}), T_m is the melting temperature of the material (K), T_{ref} is the reference temperature, normally taken as room temperature (K), and A, B, C, m and n are the material constants determined by mechanical tests.

The Johnson-Cook dynamic failure model was also used to simulate the progressive damage and failure of materials, which is expressed as follows:

$$\overline{\varepsilon}_{f}^{p} = \left[D_1 + D_2 \exp\left(D_3 \frac{p}{q}\right)\right]\left[1 + D_4 \ln\left(\frac{\dot{\overline{\varepsilon}}^{p}}{\dot{\overline{\varepsilon}}^{p}{}_{0}}\right)\right]\left[1 - D_5\left(\frac{T - T_{ref}}{T_m - T_{ref}}\right)^{\mathrm{m}}\right] \quad (2)$$

where $\overline{\varepsilon}_{f}^{p}$ is the equivalent fracture strain, p is the pressure stress, q is the Mises stress, and D_1 to D_5 are the failure parameters determined by mechanical tests.

All the material properties and temperature-dependent data are referred from the literature [71] and summarised in Table 3. It is to be noted that, since the complete deformation process is kept within dozens of nanoseconds, the thermal diffusivity distance is much shorter than the characteristic dimension of the elements in the particle and substrate, and hence the particle–substrate impact is assumed to be an adiabatic process where thermal conduction is considered to be zero during the deformation [12,18,60].

Table 3. Material properties of the Ti64 alloy used for modelling.

Nomenclature	Symbol	Unit	Value
Density	ρ	kg/m^2	4428
Specific Heat	c	J/(kg·K)	Temperature Dependent *
Melting Temperature	T_m	K	1878
Liquidus Temperature	T_L	K	1877
Solidus Temperature	T_S	K	1933
Young's Modulus	E	GPa	Temperature Dependent *
Poisson's Ratio	ν	Dimensionless	0.33
Thermal Conductivity	k	W/(m·K)	0
Latent Heat of Fusion	L_f	J/kg	365000
Inelastic Heat Fraction	η	Dimensionless	0.9
Johnson–Cook Plasticity Model	A	MPa	862
	B	MPa	331
	n	Dimensionless	0.34
	C	Dimensionless	0.012
	m	Dimensionless	0.8
	T_{ref}	K	298
	$\dot{\overline{\varepsilon}}^{p}{}_{0}$	s^{-1}	1
Johnson–Cook Dynamic Failure Model	D_1	Dimensionless	−0.09
	D_2	Dimensionless	0.25
	D_3	Dimensionless	−0.5
	D_4	Dimensionless	0.014
	D_5	Dimensionless	3.87
	T_{ref}	K	298
	$\dot{\overline{\varepsilon}}^{p}{}_{0}$	s^{-1}	1

* Temperature-dependencies were reported elsewhere [60].

3. Results and Discussion

3.1. Particle Velocity Analysis

The particle velocity of the feedstock powder impacting onto the substrate or prior deposits provides the key driving force for bonding formation, which can be derived using the following equation [72,73]:

$$v_p = \frac{1}{\frac{1}{M}\sqrt{\frac{M_w}{\gamma RT}+0.85\sqrt{\frac{d_p}{x}\sqrt{\frac{\rho_s}{p_0}}}}} \quad (3)$$

where v_p is the particle velocity, M is the local Mach number,M_w is the molar mass (28 g·mol^{-1} for N_2 and 4 g·mol^{-1} for He gas), γ is the specific heat or isentropic expansion ratio (1.67 for He and 1.4 for N_2 gas), R is the perfect gas constant (8.314 J·kmol^{-1}·K^{-1}), T is the gas temperature, d_p is the particle diameter, x is the axial position, ρ_s is the particle density, and p_0 is the gas supply pressure measured at the entrance of the nozzle.

Equation (3) would be used as a discussion tool while the numerical calculations were performed using the KSS software [54]. From the equation, it can be seen that the particle velocity is governed mainly by the molar mass (gas type), temperature and pressure of the propellant gas. By varying the gas preheated temperature and introducing gas with a lower molar mass, different particle velocities could be achieved. Figure 4a shows the calculated and measured particle velocities as well as the calculated particle temperatures as a function of gas temperature. It is observed that both the particle velocity and temperature increase with increasing gas preheated temperature. The measured particle velocity is in a good correlation with the numerical model from the KSS software [30], with a less than 4% mismatch. When the gas preheated temperature increases from 600 to 1000 °C, the measured particle velocity also increases from 697 to 800 m/s and the particle temperature (from the KSS numerical model) is raised from 339 to 625 °C. The increases in particle velocity and temperature would allow the particles to obtain high impact energy and be thermally softened to undergo the adiabatic shear instability for bonding.

The particle velocity can be further increased with the addition of He gas into the N_2 gas to form a gas mixture as shown in Figure 4b. As He gas has a molar mass of 2 g/mol while N_2 gas has a mass of 28 g/mol, by mixing these gases, the resultant N_2-He gas mixture has a lower molar mass, which can accelerate the metal particles at a higher speed as it is inversely proportional to molar mass. Every addition of 10 vol.% of He increases the overall gas velocity by approximate 20–30 m/s. This allows a further particle velocity increment within the capability of the cold-spray heater system. In addition, it would be more efficient to use the N_2-He gas mixture as the propellant gas to save cost. In relation to the cost of pure N_2 gas per m^3, the cost of the N_2-He gas mixture (for the case of N_2 with 20 vol.% He) would only cost 2-times more, while pure He gas is 6-times more expensive [39,74,75]. However, for the N_2-He gas mixture, there is a slight drop of particle temperature of around 15 °C with every 10% addition of He because He gas is a more thermally conductive gas (0.138 W/m·K) and has less thermal storage (840 kJ/m^3) compared to N_2 gas (0.0234 W/m·K, 1181.3 kJ/m^3), which will in turn slightly cool-down the powder stream by dissipating the heat during the gas expansion.

Another reason for the particle temperatures being lower is also related to the level of gas cooling in the expanding supersonic region of the nozzle. The mixed gas containing a higher fraction of He expands more (due to a higher isentropic expansion ratio) and reduces to a much lower temperature compared to the pure N_2 gas. This causes a bigger difference between the gas and the particles in addition to the difference in terms of the thermal properties of the gas and the particles.

Figure 4c shows the resultant particle velocities with respect to the pressure and temperature parameters (Table 2) when being positioned in the window of deposition, with the critical velocity

as the reference. The calculations are based on Equation (4) [27,28] and performed using the KSS software [54]. The critical velocity is expressed as

$$V_{critical} = \sqrt{\frac{F_1 \cdot 4 \cdot \sigma_{ultimate} \cdot \left(1 - \frac{T_i - T_R}{T_m - T_R}\right)}{\rho} + F_2 c_p \cdot (T_m - T_i)} \quad (4)$$

where $\sigma_{ultimate}$ is the ultimate tensile strength, ρ is the density, c_p is the heat capacity, T_m is the melting temperature, T_i is the mean temperature of particles upon impact, T_R is the reference temperature (293 K), and F_1 and F_2 are the fitting constants.

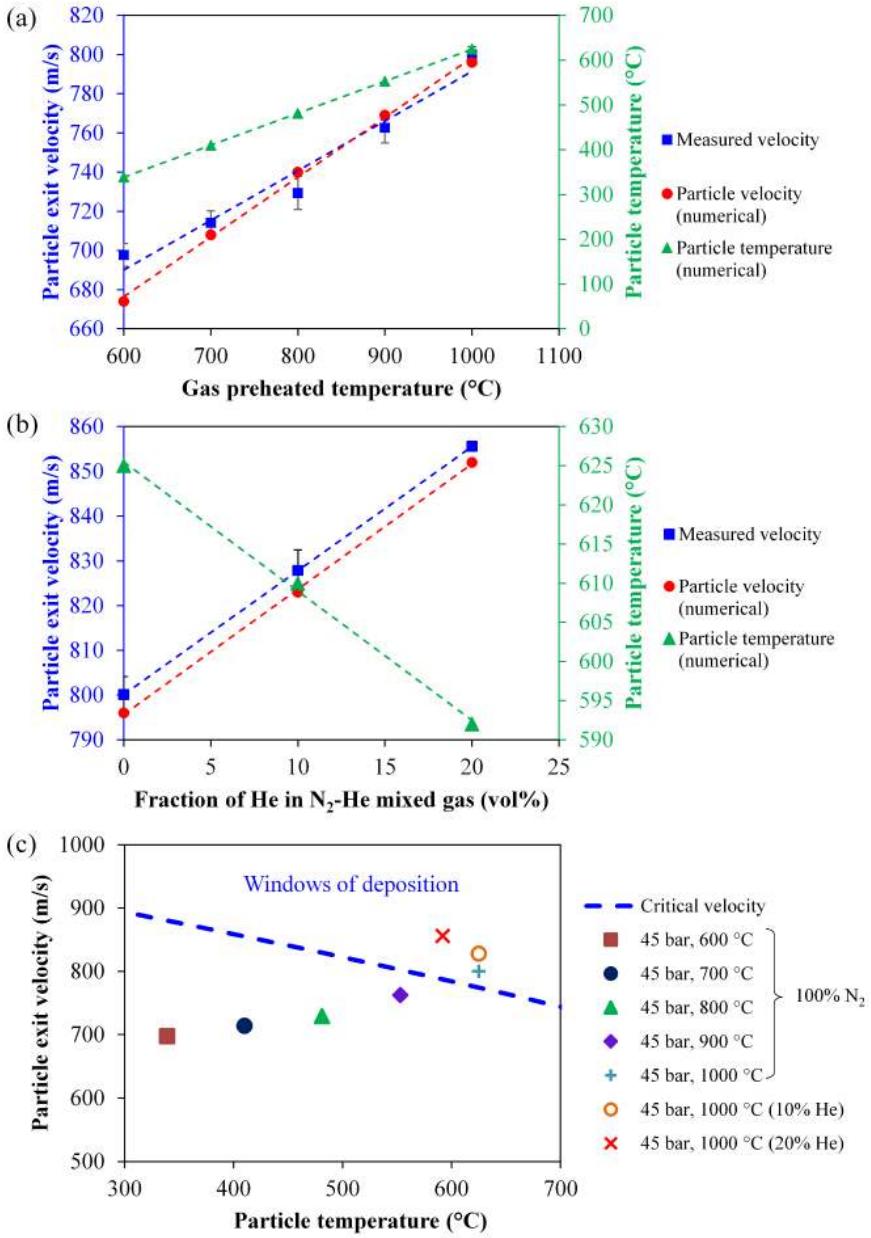

Figure 4. (**a**,**b**) The particle exit velocity as a function of (**a**) gas preheated temperature at a constant pressure of 45 bar and (**b**) fraction of He gas in N_2-He mixture (vol.%) at 45 bar and 1000 °C; and (**c**) windows of deposition based on particle velocity and temperature. The numerical calculations by Kinetic Spray Solutions (KSS) software were based on the particle size of 33 µm. It is to be noted that the velocity measurements for 45 bar, 600 and 700 °C were used as a comparison and the coatings were not actually deposited.

Equation (4) is normally referred to as the minimum particle velocity required for the formations of coating and bonding [6,18]. However, in the following sections, it will be shown that good coating adhesion can also be obtained from the particles impacted at the velocities well below the critical velocity.

3.2. Cross-Section Analysis

Figure 5a–e shows the optical micrographs of the unetched cross-sections of the Ti64 coatings deposited at different particle velocities. The porosity level of the coatings substantially drops from 11 to 1.6% (85% reduction) when the particle velocity increased from 730 to 855 m/s, as shown in Figure 5f. Besides, the current work also shows that the coating porosity level can be reduced with a small addition of He gas in the N_2 gas. The Ti64 coating sprayed with 20 vol.% addition of He gas to the N_2 gas successfully achieves a lower coating porosity in comparison with other reported works [22,42,47–49,51,76–78]. There are several reasons for the densification of the coatings: (1) the increase in particle velocity provides sufficient impact energy for the particles to deform and seal the pores, and (2) the increase in preheated temperature allows the particles to have more thermal softening. The porosity does not improve further after reaching 1.6%, which could be attributed to the reduction of particle temperature (particles are less thermally softened and thus more resistive to deformation) as a result of the He addition, which was also observed by Goldbaum et al. [44]. Some flow control parameters could be adjusted to change the particle impact temperatures by keeping particle impact velocities constant, such as (1) by extending the chamber and nozzle convergent length to increase the interaction time of particles with the preheated gas before the particles enter the nozzle throat [79]; and (2) by reducing nozzle cooling.

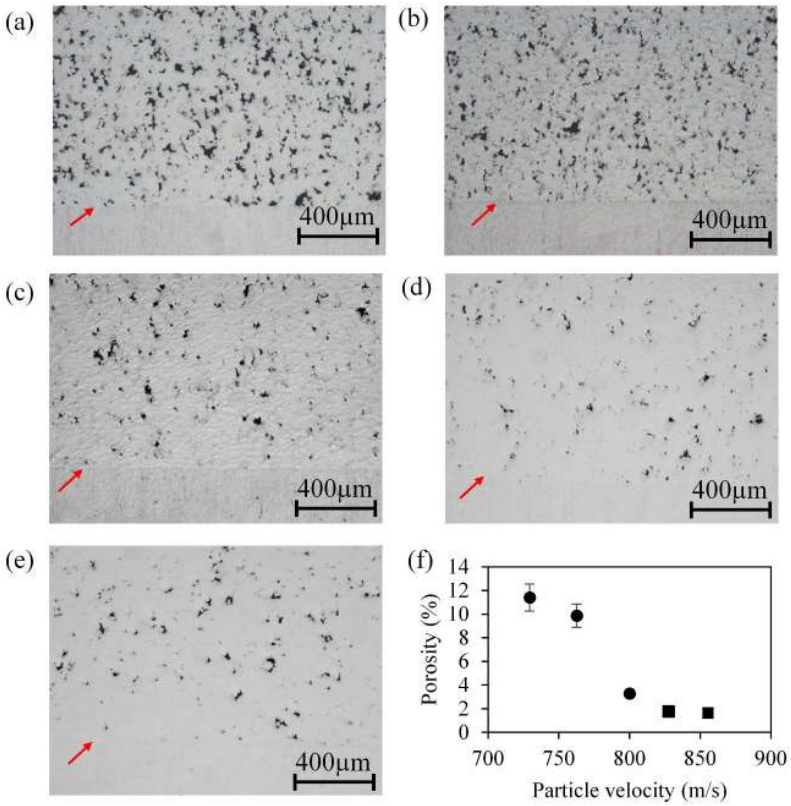

Figure 5. (**a**–**e**) Optical micrographs of polished cross-sections for the coatings deposited with particle velocities of (**a**) 730; (**b**) 760; (**c**) 800; (**d**) 827 and (**e**) 855 m/s; and (**f**) porosity level as a function of particle velocity. The arrows in (**a**–**e**) indicate the interfaces between the coatings and substrates.

Figure 6 shows the cross-sections of the Ti64 coatings deposited under increasing particle velocity. The left column of Figure 6 shows the optical micrographs of the etched cross-sections, revealing that all the coatings and substrates are intimately bonded without obvious coating delamination. It is also showed that the coated particles are more deformed at the higher particle velocity. Some of the particles in the coating deposited at 730 m/s appear to retain the spherical shape of the feedstock powder while the ones impacted at 855 m/s show higher particle flattening. The denser coating and higher flattening ratio observed in the coatings deposited with higher particle velocity result from the higher impacting energy and stronger tamping effect from the subsequent particles. On the other hand, the higher particle temperature accompanying the higher particle velocity also enhances the thermal softening of the particles, which contributes to the particle deformation and flattening. Goldbaum et al. also reported similar observations for single splats, where deformation increased with impact velocity [44].

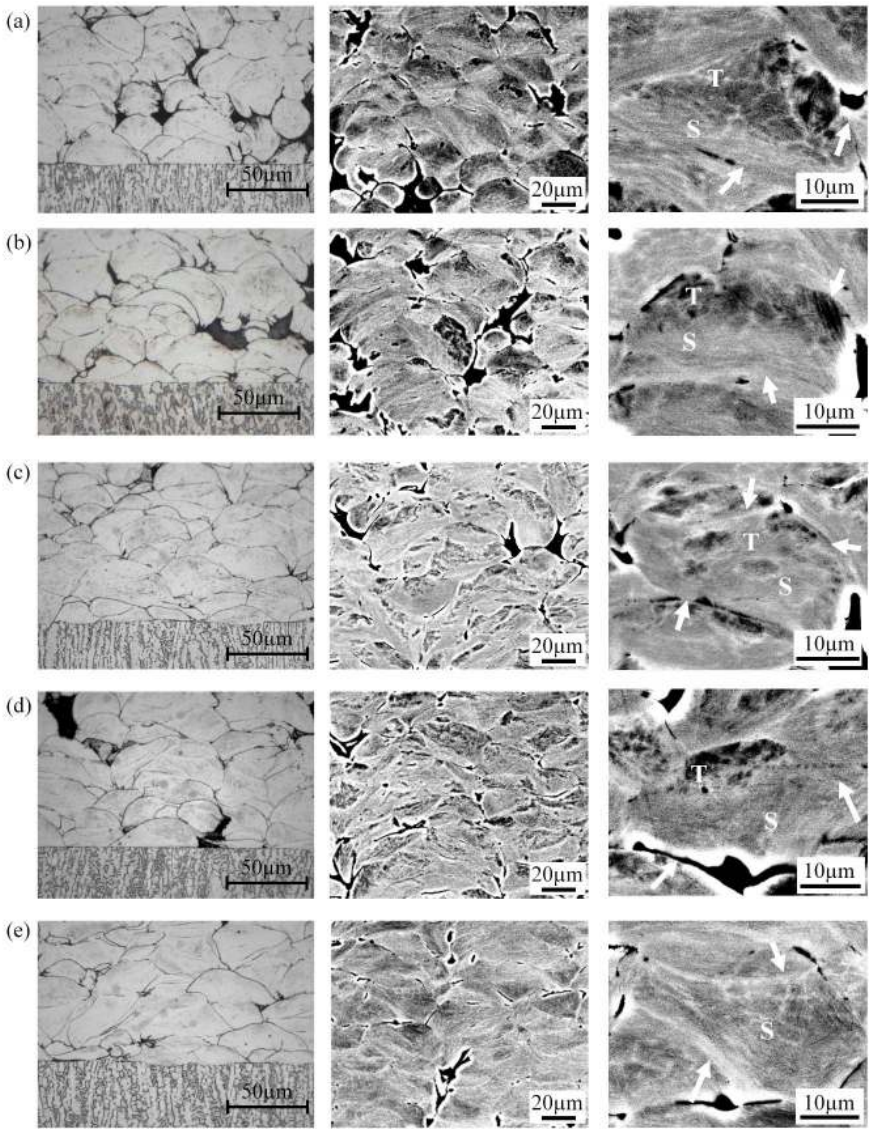

Figure 6. The etched (observed under OM; left column) and unetched cross-sections (observed under back scattered condition; middle and right columns with different magnifications) of the coatings deposited with particle velocities of (**a**) 730; (**b**) 760; (**c**) 800; (**d**) 827 and (**e**) 855 m/s under different magnifications. The textured and smooth regions are labelled with "T" and "S" in the right column, respectively where the arrows indicate the interparticle boundaries.

The middle and right columns of Figure 6 show the BEIs of the unetched coating cross-sections. The deposited Ti64 particles exhibit heterogeneous deformation, which comprises both highly and lightly deformed regions that correspond to the peripheral and interior regions of the particles, respectively [80]. The BEIs show weak electron channeling contrasts, which allow a differentiation between different grain orientations. There are mainly bimodal contrasts observed in the particles: darker (termed "textured" region) and brighter (termed "smooth" region) contrasts. The right column in Figure 6 shows the BEIs of some typical particles deposited at different particle velocities. The area of the "textured" region is found to decrease with increasing particle velocity. The ratio of the "smooth" region is also an indirect indication of the extent of grain refinement the particles have encountered. The "textured" regions are made up of more than 50% of the area of the particle deposited at the particle velocity of 730 m/s (Figure 6a) and are reduced to an approximately 50% area of the particle deposited at 760 m/s (Figure 6b). The "textured" region continues to shrink and the transition between the "textured" and "smooth" regions eventually becomes unclear as seen in the particles deposited with a velocity of 855 m/s (Figure 6e). The "textured" region is believed to be made up of broken martensitic lathes with varying degrees of fragmentation as well as the remnant martensitic microstructure from the parent powder (Figure 1b), as indicated in the difference in contrast within the region [19,48]. The "smooth" region appears rather featureless, which generally contains more refined grains than the martensitic lathes, resulting in the grain refinement of the parent microstructure due to the adiabatic shear instabilities upon impact [48,81].

The hardness of the coatings increases with particle velocity from 330 to 394 HV as shown in Figure 7. A higher particle impact velocity results in a larger deformation of the particles, and also the occurrence of adiabatic shear instability forms refined polycrystalline nanograin zones [48,81]. These refined nano-grains increase the hardness of the coating by the grain boundary strengthening effect and decrease the dislocation mobility across grain boundaries, as described in the Hall–Petch equation [82]. The hardness readings of the coatings deposited at 730 and 760 m/s have larger deviations because of the higher porosities of the coatings. In comparison to the coatings deposited at 800 to 855 m/s, the hardness is more uniform due to the much lower porosity and the more uniform deformation of the coating splats, as shown in Figure 5f. At 827 m/s (10 vol.% He in N_2-He mixed gas) and 855 m/s (20 vol.% He in N_2-He mixed gas), the hardness values reach a plateau because the increment of velocity is accompanied by a drop in temperature, where the thermal softening of the particles is insufficient to induce further deformation and overcome flow stresses for further strain hardening (or cold working).

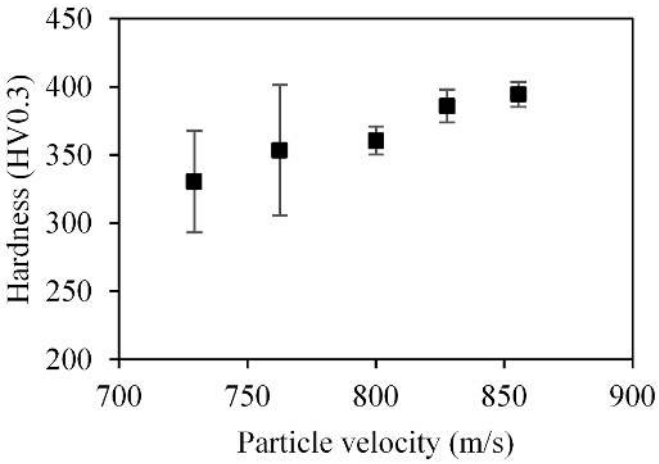

Figure 7. The hardness of coatings' cross-sections as a function of particle velocity.

3.3. Adhesion Strength

Figure 8a shows the adhesion strengths of all the coatings deposited across a large range of particle velocities tested via tensile tests (Figure 8b). It is observed that all the coatings achieve an adhesion

strength above 60 up to 65 MPa as a result of failure at the glue section (Figure 8c). The results show that the bonding at the interfaces is relatively strong (with respect to thermal spray coatings [83]), mainly resulting from metallurgical bonding and mechanical interlocking. Interestingly, the coatings deposited at 730 and 760 m/s, below the theoretical critical velocity, have reasonable good adhesion to the substrates, despite having a relatively high porosity level of around 10%. Such a high adhesion strength of porous Ti64 coatings was also reported by Perton et al. [22] (Table 1). This observation is intriguing because the coatings deposited below the critical velocity generally contain cracks and defects at the interfaces that lead to a poorer interfacial bond strength [44]. These results seem to suggest that the coating porosity would not be a limiting factor in achieving a cold sprayed coating with a high adhesion strength. The adhesion strength is often governed by the bonding quality, especially at the coating–substrate interface. It can be observed in Figure 5 that delamination between the coating and substrate is absent in all the coatings deposited with various particle velocities.

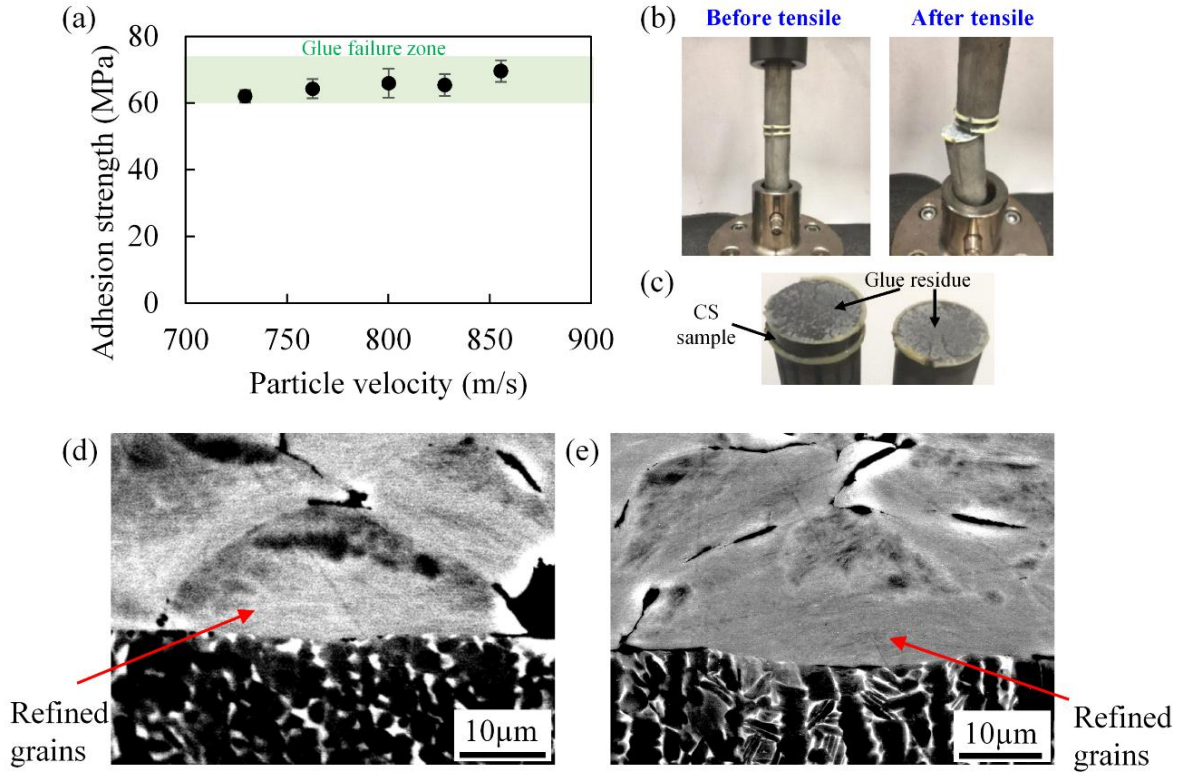

Figure 8. (**a**) Coating adhesion strength as a function of particle exit velocity; (**b**) photographs of a coated sample before and after tensile test; (**c**) photograph of the coated sample which shows glue failure, and (**d**,**e**) back-scattered SEM micrographs of particles impacted with velocities of (**d**) 730 and (**e**) 800 m/s.

The high adhesion strength of the porous Ti64 coatings deposited at 730 and 760 m/s could be attributed to the grain refinement at the impact zone, despite being not so severely deformed as those particles impacted at 800 to 855 m/s. The similarity of the grain refinement locations of particles deposited at 730 and 800 m/s is shown in Figure 8d,e, where these refined grains may have interlocked with the substrate surface, which has also refined the grains from the bombardment of the Ti64 particles [84], forming a bond strength higher than 60 MPa. Another possible reason for this high bonding strength was the polished substrate surface condition that allows the particles with a lower impact velocity to bond with the substrate without surface barriers [22,24].

The particles are able to efficiently convert the impact energy (kinetic energy) to plastic strain and thermal energy. The impact energy allows the particles to form the classic adiabatic shear instability feature, where the high interfacial temperature (near melting point) would induce a reduction in flow

stress and allow the material to flow with a high strain (jetting). The polished surface does not contain the features that prevent the formation of material jetting. In an event of a rough surface, the particles would have utilised the impact energy to conform or deform the features, which might induce the lower strain energy to be redistributed as thermal energy for bonding [22]. The evolutions of stress, strain and temperature will be further discussed in Section 3.5.

3.4. Fractography

To understand the bonding between the particle–substrate and particle–particle, the coatings were forcibly fractured by shear and bending at the coating–substrate interfaces and cross-sections, respectively. The SEM images in Figure 9 give an overview (left column) of the substrate surfaces after the coatings are removed and the individual impact craters on the substrates (right column). An impact crater is typically a cup-like feature associated with a rim of dimple fracture. Three significant regions could be identified from each of the craters: (i) the core of the crater, which generally refers to the impact centre ("south pole" [18]) where the impact particle bounces off the substrate; (ii) the rim of the dimple fracture, which corresponds to the periphery of impacted particle; and (iii) the outermost region, or the material-jetting portion [84]. It is observed that both the core and outermost region of the craters are generally featureless, indicating the absence of metallurgical bonding and occurrence of brittle failure. On the contrary, the dimple fracture is representative of ductile failure, which is believed to occur at the metallurgically bonded and/or mechanically interlocked periphery of a particle with its contact surfaces. Some particles are also found to be retained on the substrates as a result of greater particle–substrate interfacial bonding than the interparticle bonding. The broken of section could be the refined grains sections as they might be less ductile due to grain boundary strengthening, and more susceptible to crack upon force.

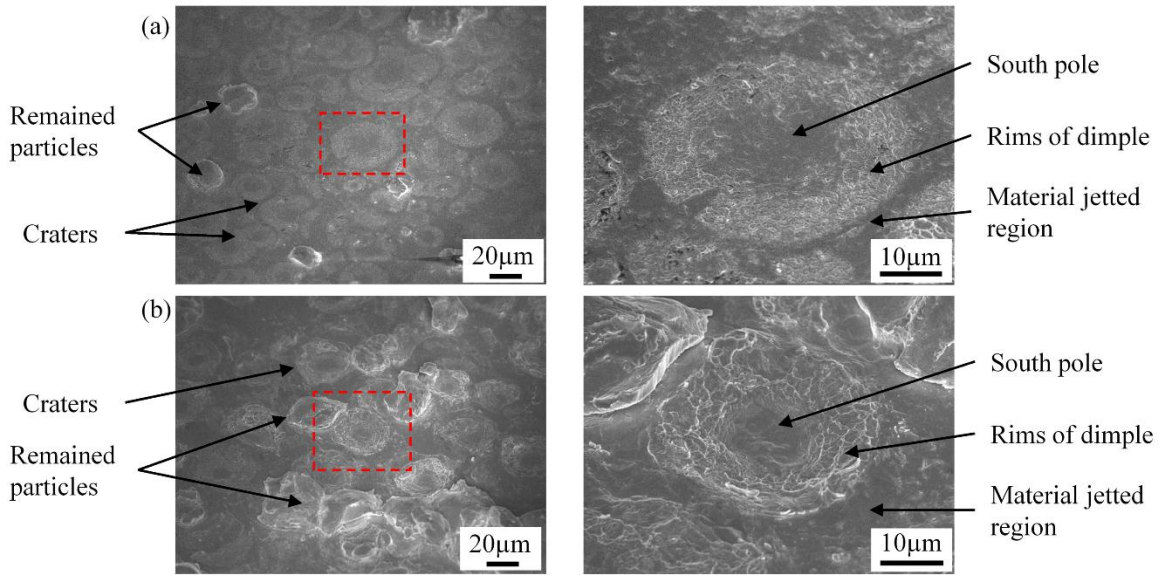

Figure 9. SEM micrographs of fractured interfaces on the substrate side for the coatings deposited at particle velocities of (**a**) 730 and (**b**) 855 m/s, observed under different magnifications at a tilted angle of 45°. The fractured interfaces of the other velocities are shown in Figure S1 (Supplementary Materials).

For the coating deposited at the particle velocity of 730 m/s, as shown in Figure 9a, very few particles remain on the substrate surface, resulting in a nearly clean cleavage of the coating from the substrate. The impact craters are also shallow due to the lower impact energy. However, the rim of the crater shows a dimple fracture, which is believed to account for the reasonably high adhesion strength (glue failure). This suggests that a high bond strength still be attained even at a lower particle velocity. In comparison, for a higher particle velocity, i.e., 855 m/s (Figure 9b), there are an increasing number

of particles that are retained by the substrate as well as the deeper craters due to the higher particle impact energy. The rims of the dimple fracture also become wider and thicker with increasing particle velocity, which indicates a larger bonded region of the particle to the substrate.

Figure 10a,b show the overview of the fractured interface (coating side) of the coating deposited at particle velocities of 730 and 855 m/s after being removed from the substrate and the individual protrusion found on the coating, respectively. The rims of the dimple fracture in the particle protrusions at the bonded regions correspond to the rims of the craters on the substrate side. The outer boundary of the dimple fractures is the jetted region of the particle. This indicates that the bonding resulting from the adiabatic shear instability mainly occurs in the periphery region of the particle, as reported by Vidaller et al. [45]. The particle protrusion height indicates the extent of particle penetration into the substrate. Therefore, the dimple fracture region becomes wider and the protrusion height becomes more substantial alongside a high particle velocity of 855 m/s, as shown in Figure 10b. The coatings and the particle protrusions from the coatings deposited with other particle velocities are also available for comparison in Figure S2 (Supplementary Materials).

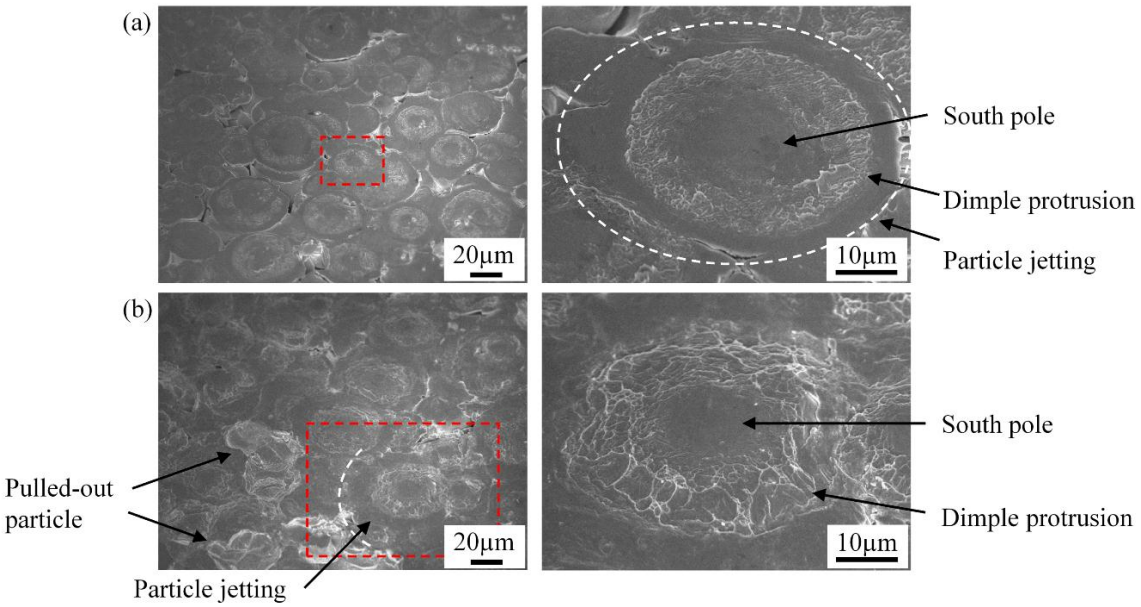

Figure 10. SEM micrographs of the fractured interfaces on the coating side for the coatings deposited at particle velocities of (**a**) 730 and (**b**) 855 m/s, observed under different magnifications at a tilted angle of 45°. The fractured interfaces of the coatings deposited with the sprayed particles of other impact velocities are shown in Figure S2 (Supplementary Materials).

As shown in Figure 11, the fractured cross-sections of the Ti64 coatings are also investigated to understand the interparticle bonding in the coatings. Figure 11a–c show the overview of the fractured coatings deposited at 730, 800 and 855 m/s, respectively. The particles coated at 730 m/s appear to partially retain the spherical shape while the particles coated at 800 and 855 m/s are significantly flattened in the impact direction. The severe plastic deformation allows the particles to seal up the interparticle gaps more effectively as a result of the stronger tamping effect at higher particle impact, and eventually densifies the coatings. The cleaved surfaces of the particles sprayed at 730 m/s (Figure 11a) show a large smooth and clean delaminated area (from particles) and some dimple fracture. At the high particle velocities of 800 m/s (Figure 11b), and 855 m/s (Figure 11c), the amount of dimple fracture increases substantially. For comparison, the SEM images of the fractured coatings deposited at other particle velocities are shown in Figure S3 (Supplementary Materials).

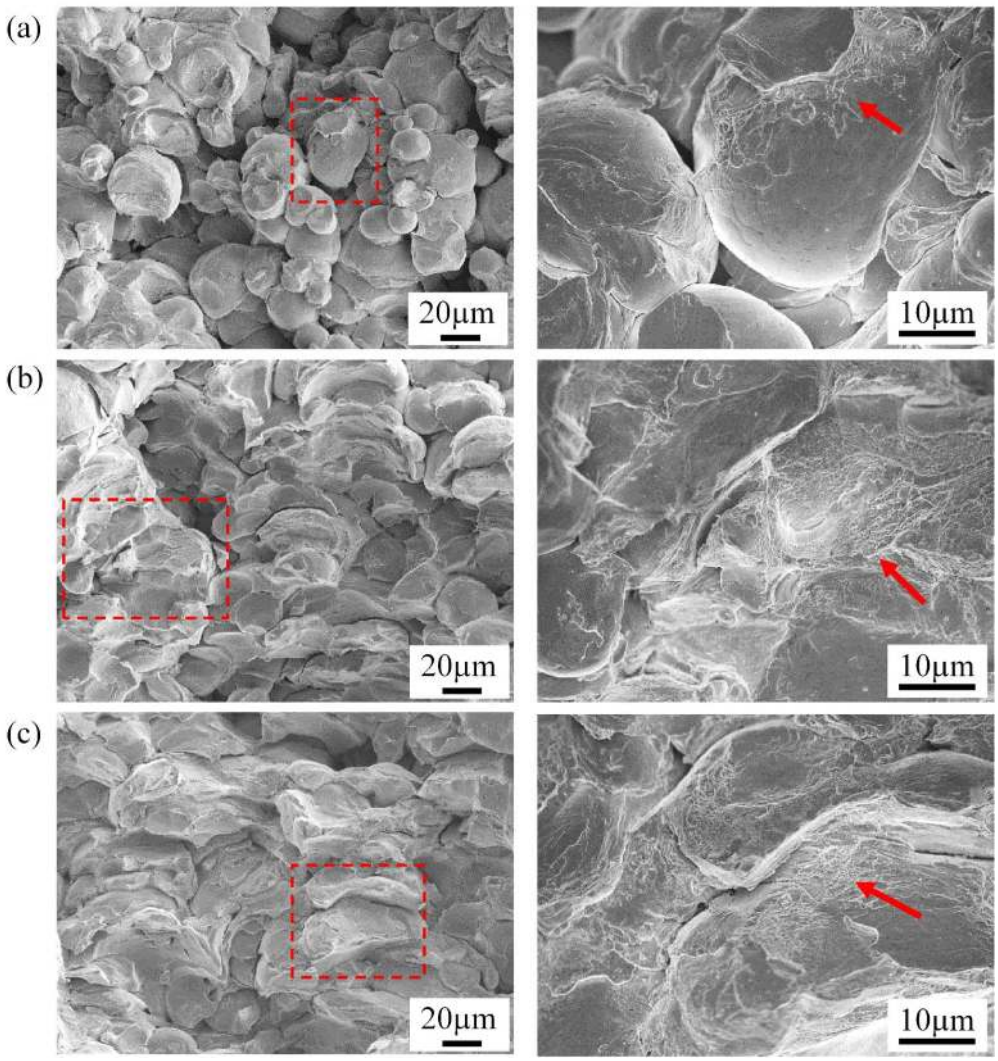

Figure 11. SEM micrographs with different magnifications showing fractured cross-sections of the coatings deposited with particle velocities of (**a**) 730; (**b**) 800 and (**c**) 855 m/s. The fractured cross-sections of the coatings with respect to other particle velocities are shown in Figure S3 (Supplementary Materials).

3.5. Finite Element Model

The finite element modelling (FEM) is carried out to understand the particle impact phenomena at different particle velocities. The overview of the impact is shown in Figure 12 with the evolutions of the elements A, B and C in terms of temperature, stress and strain at 30 ns upon impact. At 30 ns, these regions undergo a clear jump (termed "secondary" jump) in their temperature profiles, where the adiabatic shear instability takes place and aids in interfacial bonding [12], as reported in a previous work [61]. For the case of 730 m/s, the top section of the particle is relatively colder (ranging from 750 to 900 K) as compared to the interface (900 to 1400 K). The temperature at the interface increases from the middle of the particle (element A, 887 K) towards the periphery (element C, 1333 K), as shown in Figure 13a. The temperature rise at the interface periphery (element C) to as high as 0.7 T_m of Ti64 (refer to Table 3) will soften the material and reduce the flow stress from 800 to 480 MPa as compared to element A (almost no stress reduction) and B (800 to 750 MPa), as shown in Figure 13b. With a lower flow stress, the particle periphery (element C) deforms as high as 400% in strain compared to the central regions (elements A and B) shown in Figure 13c.

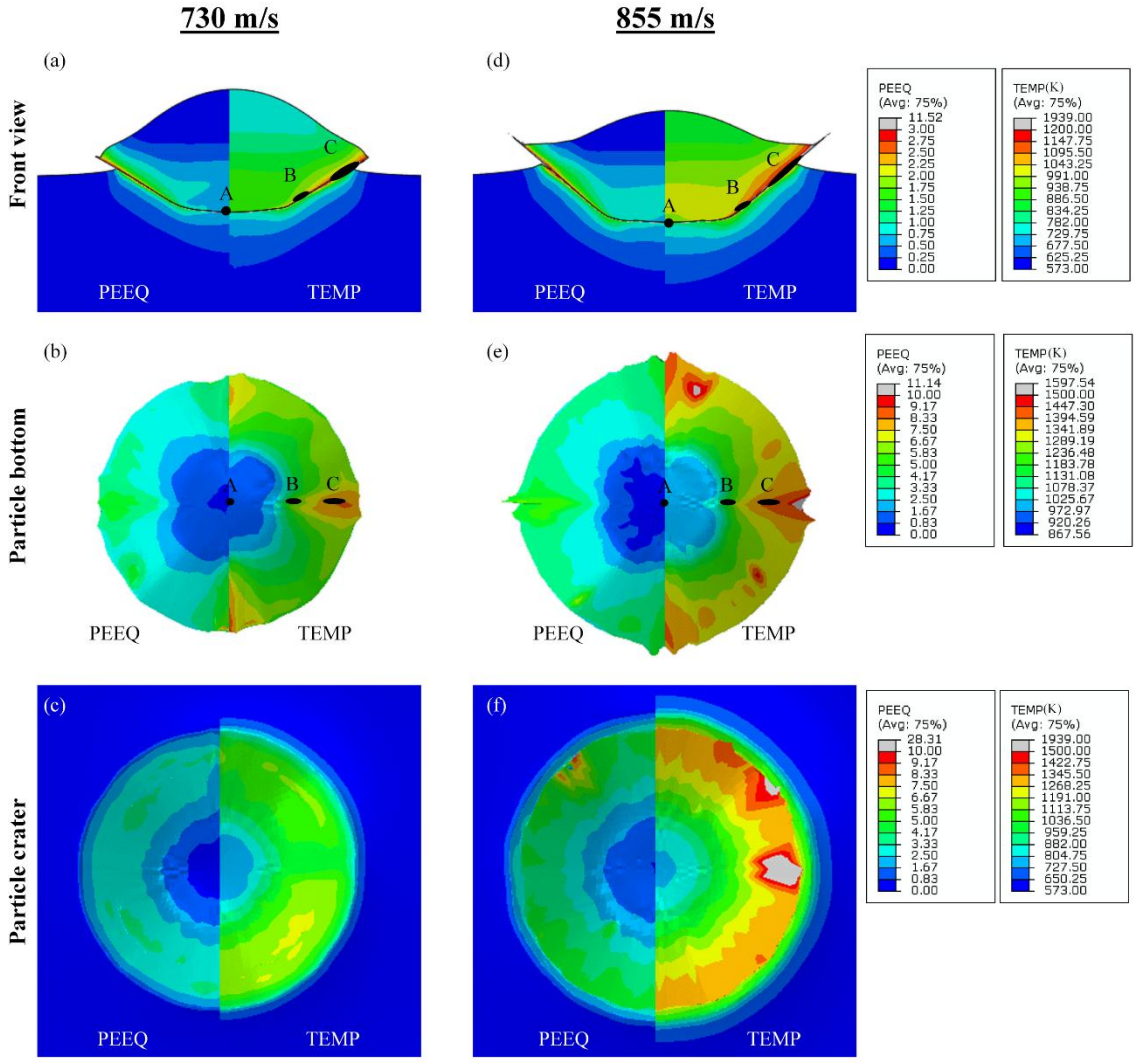

Figure 12. Simulated deformation and temperature profiles of a sprayed Ti64 particle impacted on a Ti64 substrate at velocities of (**a**–**c**) 730 m/s and (**d**–**f**) 855 m/s at 30 ns with (**a**,**d**) front view, (**b**,**e**) bottom view, and (**c**,**f**) crater view.

The particle impact at 855 m/s shows a substantial increase in temperature, flow stress reduction and strain as compared to the particle impacted at 730 m/s. A larger portion in the particle experienced a higher temperature. The temperature at the interface periphery (element C) reaches 1412 K (as high as 0.75 T_m) (Figure 13d), further reducing the flow stress from 718 to 406 MPa (Figure 13e). Both the initial and the subsequent stresses are lower than the stress of particle impacted at 730 m/s due to thermal softening. As a result, the particle deformation is more severe and achieves a strain of 440% at its periphery (element C), while elements B and A record strains of 295% and 74%, respectively, as shown in Figure 13f.

Both impact phenomena at 730 and 855 m/s do show the occurrence of the adiabatic shear instability because there is a high jump of temperature (0.7 to 0.75 T_m) and a significant drop of stress (around 50% drop) occurring in the material [85], as predicted by the modelling results (Figure 13). However, from the experimental observations and the simulated particle shape upon impact (Figure 12), it can be seen that a much lower extent of material jetting happens in the case of 730 m/s in particle velocity, which might limit the particle–substrate adhesion. In the case of low particle velocity, the particle adhesion could be promoted by using the optimised process parameters such as smooth and preheated surfaces, optimum traverse scan speed, raster steps, etc. For comparison, the FEM of particle impact at 800 m/s is also shown in Figure S4 (Supplementary Materials). The increases

in temperature strain and reduction of flow stress are slightly higher than the particle impacted at 855 m/s due to the higher initial temperature before the impact. The overall adhesion of the coating deposited with the particles sprayed below the critical velocity could primarily be attributed to the velocity distribution of the particles propelled by the gas stream, wherein the material jetting occurs in a relatively small fraction of particles, to facilitate the particle–substrate bonding with the velocities higher than the average velocity (in the case of 730 m/s, which is lower than the predicted critical velocity). For a 855 m/s mean particle velocity, a much higher fraction of particles experience material jetting and hence resulting in better bonding and lower porosity in the coating in general.

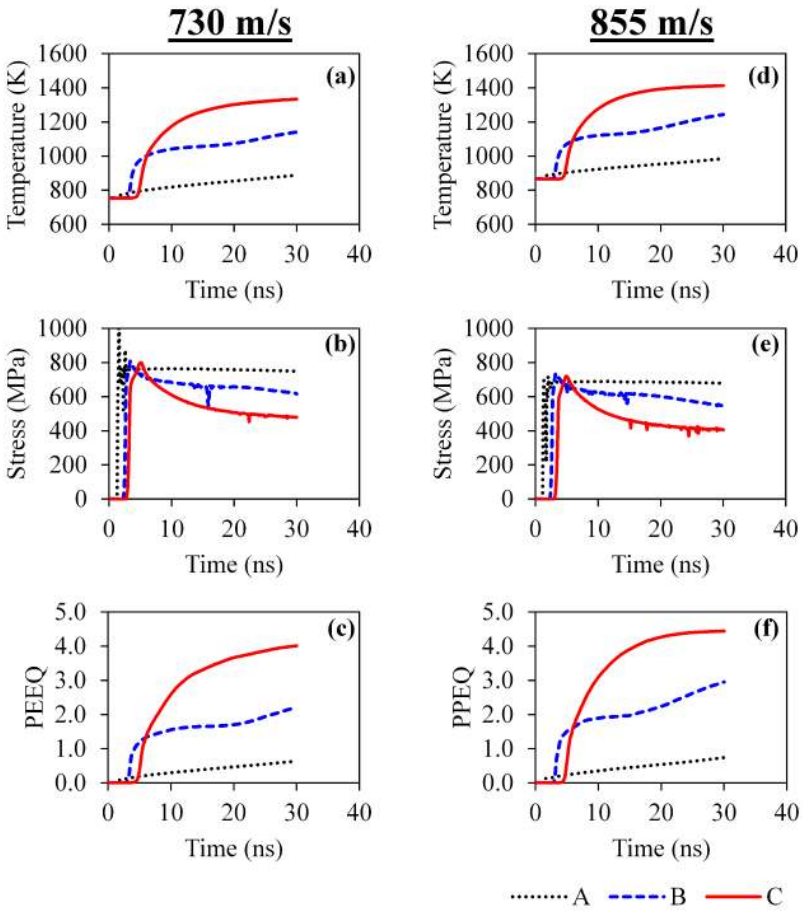

Figure 13. Stress, strain and temperature evolutions of elements A, B and C (as shown in Figure 12) at the Ti64 particle interface when impacted with velocities of (**a**–**c**) 730 and (**d**–**f**) 855 m/s for the duration of 30 ns.

The FEMs with respect to 730 and 855 m/s can be correlated back to the microstructure and mechanical properties of the coatings. The decrease in porosity with increased velocity is because of a higher particle deformation, with up to 440% strain due to thermal softening. However, the porosity of the cold-sprayed Ti64 coatings is not further reduced beyond the particle velocities of 827 and 855 m/s because a higher fraction of He gas in the N_2-He mixture has a cooling effect on the particles. To further reduce the coating porosity level, for example, by around 1 to 2% (Table 1), the particles have to be deposited at a velocity of 900 m/s or above that is only achievable when using pure He gas, which may not be economical due to the high cost of He gas.

Besides this, a higher particle impact velocity results in more grain refinement via the serration of large grains in the textured region into more refined grains in the smooth region. From the simulation, it is evident that the particle impacted at 855 m/s would have more grain refinement than that impacted at 730 m/s because of the higher deformation and temperatures observed at the particle–substrate

interface in the former case. The grain refinement would increase the surface area of the grains to bond with the neighbouring grains from other particles to form a strong bonding [86]. This can be observed in the increasing quantity, width and thickness of the dimple fractures remaining on the adhered particles and substrate surfaces of the fractured samples (Section 3.4). The particle deposited at 730 m/s reveals that the periphery of the particle experiences a temperature rise to 0.7 T_m and strain of 400%, ensuring sufficient metallurgical bonding to achieve an adhesion strength of at least 60 MPa (Section 3.3).

4. Conclusions

The deposition of cold-sprayed Ti64 coatings on Ti64 substrates at different particle impact velocities was investigated experimentally and simulated with finite element modelling (FEM). The following conclusions were drawn based on the results obtained from the study:

- The addition of He gas into N_2 gas efficiently increased the particle velocities without a significant reduction in particle temperature, which contributed to the thermal softening and plastic deformation of the sprayed particles;
- The porosity content in the Ti64 coatings dropped from about 11 to 1.6% with increasing particle velocity from 730 to 855 m/s;
- The coating/substrate interfaces of all the coatings were intimate without macroscopic cracks. The percentage of smooth regions (consisted of refined nanograins) of the coatings increased with higher particle velocity as compared to the textured regions (consisted of martensite laths) due to the severe particle deformation that helped with particle refinement;
- The microhardness of the coatings increased with higher particle velocity due to a higher fraction of refined grains (grain boundary strengthening) within the splats;
- The adhesion strengths of all the coatings deposited across the velocity range exceeded 60 MPa, as the tests failed at the glue regions, which showed that an effective coating with an appreciable adhesion strength, albeit with a higher porosity level, could be formed even with a particle velocity lower than the calculated critical velocity. This could be attributed to the velocity distribution of particles where a fraction of particles could have velocities higher than the respective critical velocities to form a strong bonding with the substrate, coupled with the optimum deposition parameters;
- Fractographic analyses revealed that the dimple fractures were more prominent in the coatings deposited at higher particle impact velocities due to the more severe cohesive failure within particles;
- The FEM indicated more plastic deformation and higher temperatures at the peripheries of the particle with a higher impact velocity (e.g., 855 m/s), which correlated well with the experimental observation of the mechanical response of the coatings;
- The use of an N_2-He gas mixture as the propellant gas was more cost effective for producing high quality coatings.

Supplementary Materials: The following are available online at http://www.mdpi.com/2079-6412/8/9/327/s1, Figure S1: SEM micrographs of fractured interfaces on the substrate side for the coatings deposited at particle velocities of (a) 760, (b) 800 and (c) 827 m/s, observed under different magnifications at a tilted angle of 45°; Figure S2: SEM micrographs of fractured interfaces on the coating side for the coatings deposited at particle velocities of (a) 760, (b) 800, (c) 827 m/s observed under different magnifications at a tilted angle of 45°; Figure S3: SEM micrographs of fractured cross-sections of the coatings deposited at particle velocities of (a) 760 and (b) 827 m/s under different magnifications; Figure S4: (a–c) Simulated deformation and temperature profiles of a Ti64 particle impacted on a Ti64 substrate at particle velocity of 800 m/s at 30 ns for different views and (d–f) temperature, stress and strain evolutions of elements A, B and C at the interfaces of Ti64 particle impacted at 800 m/s, for the duration of 30 ns.

Author Contributions: Conceptualization, A.W.-Y.T. and E.L; Methodology, A.W.-Y.T., J.Y.L. and W.S., Software, X.S. and W.Z.; Investigation, A.W.-Y.T., J.Y.L. and W.S.; Resources, F.L., C.B.B. and Z.D.; Writing-Original Draft Preparation, A.W.-Y.T.; Writing-Review & Editing, A.W.-Y.T., J.Y.L., A.B. and E.L.; Supervision, E.L.; Project Administration, E.L. and I.M.; Funding Acquisition, E.L. and I.M.

Funding: This work was financially supported by the National Research Foundation (NRF), Rolls-Royce (RR) and Nanyang Technological University (NTU), Singapore with the research grant (M-RT3.1: Metal Cold Spray).

Acknowledgments: Authors acknowledged the Facility for Analysis, Characterisation, Testing and Simulation (FACTS), Nanyang Technological University (NTU), for use of their electron microscopy facilities.

Conflicts of Interest: The authors declare no conflict of interest.

References

1. Boyer, R.R. An overview on the use of titanium in the aerospace industry. *Mater. Sci. Eng. A* **1996**, *213*, 103–114. [CrossRef]
2. Kalla, G. CO_2-laser beam welding of structural steel with a thickness up to 20 mm. *Rev. Métall.* **1996**, *93*, 1303–1310. [CrossRef]
3. Wang, X.B. Temperature distribution in adiabatic shear band for ductile metal based on Johnson-Cook and gradient plasticity models. *Trans. Nonferrous Met. Soc. Chin.* **2006**, *16*, 333–338. [CrossRef]
4. Yilbas, B.S.; Sami, M.; Nickel, J.; Coban, A.; Said, S.A.M. Introduction into the electron beam welding of austenitic 321-type stainless steel. *J. Mater. Process. Technol.* **1998**, *82*, 13–20. [CrossRef]
5. Champagne, V.K. *The Cold Spray Materials Deposition Process: Fundamentals and Applications*; CRC Press: Boca Raton, FL, USA, 2007.
6. Papyrin, A.; Kosarev, V.; Klinkov, S.; Alkhimov, A.; Fomin, V.M. *Cold Spray Technology*, 1st ed.; Elsevier: Amsterdam, The Netherlands, 2007.
7. Dykhuizen, R.C.; Smith, M.F.; Gilmore, D.L.; Neiser, R.A.; Jiang, X.; Sampath, S. Impact of high velocity cold spray particles. *J. Therm. Spray Technol.* **1999**, *8*, 559–564. [CrossRef]
8. Vlcek, J.; Gimeno, L.; Huber, H.; Lugscheider, E. A systematic approach to material eligibility for the cold-spray process. *J. Therm. Spray Technol.* **2005**, *14*, 125–133. [CrossRef]
9. McCune, R.C.; Papyrin, A.N.; Hall, J.N.; Riggs, W.L.I.; Zajchowski, P.H. An exploration of the cold gas-dynamic spray method for several materials systems. In Proceedings of the 8th National Thermal Spray Conference, Houston, TX, USA, 11–15 September 1995; p. 795.
10. Kosarev, V.F.; Klinkov, S.V.; Alkhimov, A.P.; Papyrin, A.N. On some aspects of gas dynamics of the cold spray process. *J. Therm. Spray Technol.* **2003**, *12*, 265–281. [CrossRef]
11. Schmidt, T.; Gaertner, F.; Kreye, H. New developments in cold spray based on higher gas and particle temperatures. *J. Therm. Spray Technol.* **2006**, *15*, 488–494. [CrossRef]
12. Grujicic, M.; Zhao, C.L.; DeRosset, W.S.; Helfritch, D. Adiabatic shear instability based mechanism for particles/substrate bonding in the cold-gas dynamic-spray process. *Mater. Des.* **2004**, *25*, 681–688. [CrossRef]
13. Bae, G.; Kumar, S.; Yoon, S.; Kang, K.; Na, H.; Kim, H.J.; Lee, C. Bonding features and associated mechanisms in kinetic sprayed titanium coatings. *Acta Mater.* **2009**, *57*, 5654–5666. [CrossRef]
14. Bae, G.; Xiong, Y.; Kumar, S.; Kang, K.; Lee, C. General aspects of interface bonding in kinetic sprayed coatings. *Acta Mater.* **2008**, *56*, 4858–4868. [CrossRef]
15. Alkhimov, A.P.; Klinkov, S.V.; Kosarev, V.F.; Papyrin, A.N. Gas-dynamic spraying study of a plane supersonic two-phase jet. *J. Appl. Mech. Tech. Phys.* **1997**, *38*, 324–330. [CrossRef]
16. Dykhuizen, R.C.; Smith, M.F. Gas dynamic principles of cold spray. *J. Therm. Spray Technol.* **1998**, *7*, 205–212. [CrossRef]
17. Gilmore, D.L.; Dykhuizen, R.C.; Neiser, R.A.; Smith, M.F.; Roemer, T.J. Particle velocity and deposition efficiency in the cold spray process. *J. Therm. Spray Technol.* **1999**, *8*, 576–582. [CrossRef]
18. Assadi, H.; Gärtner, F.; Stoltenhoff, T.; Kreye, H. Bonding mechanism in cold gas spraying. *Acta Mater.* **2003**, *51*, 4379–4394. [CrossRef]
19. Kim, K.; Watanabe, M.; Kawakita, J.; Kuroda, S. Grain refinement in a single titanium powder particle impacted at high velocity. *Scr. Mater.* **2008**, *59*, 768–771. [CrossRef]
20. Luo, X.T.; Li, C.X.; Shang, F.L.; Yang, G.J.; Wang, Y.Y.; Li, C.J. High velocity impact induced microstructure evolution during deposition of cold spray coatings: A review. *Surf. Coat. Technol.* **2014**, *254*, 11–20. [CrossRef]

21. Cavaliere, P.; Silvello, A. Processing parameters affecting cold spay coatings performances. *Int. J. Adv. Manuf. Technol.* **2014**, *71*, 263–277. [CrossRef]
22. Perton, M.; Costil, S.; Wong, W.; Poirier, D.; Irissou, E.; Legoux, J.G.; Blouin, A.; Yue, S. Effect of pulsed laser ablation and continuous laser heating on the adhesion and cohesion of cold sprayed Ti-6Al-4V coatings. *J. Therm. Spray Technol.* **2012**, *21*, 1322–1333. [CrossRef]
23. Sun, W.; Tan, A.W.Y.; Bhowmik, A.; Marinescu, I.; Song, X.; Zhai, W.; Li, F.; Liu, E. Deposition characteristics of cold sprayed Inconel 718 particles on Inconel 718 substrates with different surface conditions. *Mater. Sci. Eng. A* **2018**, *720*, 75–84. [CrossRef]
24. Sun, W.; Tan, A.W.Y.; Khun, N.W.; Marinescu, I.; Liu, E. Effect of substrate surface condition on fatigue behavior of cold sprayed Ti6Al4V coatings. *Surf. Coat. Technol.* **2017**, *320*, 452–457. [CrossRef]
25. Bhattiprolu, V.S.; Johnson, K.W.; Ozdemir, O.C.; Crawford, G.A. Influence of feedstock powder and cold spray processing parameters on microstructure and mechanical properties of Ti-6Al-4V cold spray depositions. *Surf. Coat. Technol.* **2018**, *335*, 1–12. [CrossRef]
26. Binder, K.; Gottschalk, J.; Kollenda, M.; Gärtner, F.; Klassen, T. Influence of impact angle and gas temperature on mechanical properties of titanium cold spray deposits. *J. Therm. Spray Technol.* **2011**, *20*, 234–242. [CrossRef]
27. Schmidt, T.; Gärtner, F.; Assadi, H.; Kreye, H. Development of a generalized parameter window for cold spray deposition. *Acta Mater.* **2006**, *54*, 729–742. [CrossRef]
28. Schmidt, T.; Assadi, H.; Gärtner, F.; Richter, H.; Stoltenhoff, T.; Kreye, H.; Klassen, T. From particle acceleration to impact and bonding in cold spraying. *J. Therm. Spray Technol.* **2009**, *18*, 794–808. [CrossRef]
29. Huang, R.; Fukanuma, H. Study of the influence of particle velocity on adhesive strength of cold spray deposits. *J. Therm. Spray Technol.* **2012**, *21*, 541–549. [CrossRef]
30. List, A.; Gärtner, F.; Mori, T.; Schulze, M.; Assadi, H.; Kuroda, S.; Klassen, T. Cold spraying of amorphous Cu50Zr50 alloys. *J. Therm. Spray Technol.* **2015**, *24*, 108–118. [CrossRef]
31. Kumar, S.; Bae, G.; Kang, K.; Yoon, S.; Lee, C. Effect of powder state on the deposition behaviour and coating development in kinetic spray process. *J. Phys. D Appl. Phys.* **2009**, *42*, 075305. [CrossRef]
32. Marrocco, T.; McCartney, D.G.; Shipway, P.H.; Sturgeon, A.J. Production of titanium deposits by cold-gas dynamic spray: Numerical modeling and experimental characterization. *J. Therm. Spray Technol.* **2006**, *15*, 263–272. [CrossRef]
33. Wong, W.; Irissou, E.; Ryabinin, A.N.; Legoux, J.-G.; Yue, S. Influence of helium and nitrogen gases on the properties of cold gas dynamic sprayed pure titanium coatings. *J. Therm. Spray Technol.* **2011**, *20*, 213–226. [CrossRef]
34. Li, C.-J.; Li, W.-Y.; Liao, H. Examination of the critical velocity for deposition of particles in cold spraying. *J. Therm. Spray Technol.* **2006**, *15*, 212–222. [CrossRef]
35. Meyer, M.; Yin, S.; Lupoi, R. Particle in-flight velocity and dispersion measurements at increasing particle feed rates in cold spray. *J. Therm. Spray Technol.* **2017**, *26*, 60–70. [CrossRef]
36. Yin, S.; Liu, Q.; Liao, H.L.; Wang, X.F. Effect of injection pressure on particle acceleration, dispersion and deposition in cold spray. *Comput. Mater. Sci.* **2014**, *90*, 7–15. [CrossRef]
37. Zahiri, S.H.; Yang, W.; Jahedi, M. Characterization of cold spray titanium supersonic jet. *J. Therm. Spray Technol.* **2009**, *18*, 110–117. [CrossRef]
38. Li, W.Y.; Liao, H.; Douchy, G.; Coddet, C. Optimal design of a cold spray nozzle by numerical analysis of particle velocity and experimental validation with 316L stainless steel powder. *Mater. Des.* **2007**, *28*, 2129–2137. [CrossRef]
39. Ozdemir, O.C.; Widener, C.A.; Helfritch, D.; Delfanian, F. Estimating the effect of helium and nitrogen mixing on deposition efficiency in cold spray. *J. Therm. Spray Technol.* **2016**, *25*, 660–671. [CrossRef]
40. Wu, X.K.; Zhou, X.L.; Wang, J.G.; Zhang, J.S. Numerical investigation on acceleration of gaseous mixture of nitrogen and helium on particles during cold spraying. *J. Mater. Eng.* **2010**, *8*, 12–15.
41. Irissou, E.; Ilinca, F.; Wong, W.; Legoux, J.; Yue, S. Investigation on the effect of helium-to-nitrogen ratio as propellent gas mixture on the processing of titanium coating using cold gas dynamic spray. In Proceedings of the International Thermal Spray Conference (ITSC 2011), Hamburg, Germany, 27–29 September 2011; Volume 276, pp. 88–93.
42. Khun, N.W.; Tan, A.W.Y.; Bi, K.J.W.; Liu, E. Effects of working gas on wear and corrosion resistances of cold sprayed Ti-6Al-4V coatings. *Surf. Coat. Technol.* **2016**, *302*, 1–12. [CrossRef]

43. Sun, W.; Tan, A.W.Y.; Marinescu, I.; Toh, W.Q.; Liu, E. Adhesion, tribological and corrosion properties of cold-sprayed CoCrMo and Ti6Al4V coatings on 6061-T651 Al alloy. *Surf. Coat. Technol.* **2017**, *326*, 291–298. [CrossRef]
44. Goldbaum, D.; Shockley, J.M.; Chromik, R.R.; Rezaeian, A.; Yue, S.; Legoux, J.G.; Irissou, E. The effect of deposition conditions on adhesion strength of Ti and Ti6Al4V cold spray splats. *J. Therm. Spray Technol.* **2011**, *21*, 288–303. [CrossRef]
45. Vidaller, M.V.; List, A.; Gaertner, F.; Klassen, T.; Dosta, S.; Guilemany, J.M. Single impact bonding of cold sprayed Ti-6Al-4V powders on different substrates. *J. Therm. Spray Technol.* **2015**, *24*, 644–658. [CrossRef]
46. Vo, P.; Irissou, E.; Legoux, J.G.; Yue, S. Mechanical and microstructural characterization of cold-sprayed Ti-6Al-4V after heat treatment. *J. Therm. Spray Technol.* **2013**, *22*, 954–964. [CrossRef]
47. Luo, X.T.; Wei, Y.K.; Wang, Y.; Li, C.J. Microstructure and mechanical property of Ti and Ti6Al4V prepared by an in situ shot peening assisted cold spraying. *Mater. Des.* **2015**, *85*, 527–533. [CrossRef]
48. Birt, A.M.; Champagne, V.K.; Sisson, R.D.; Apelian, D. Microstructural analysis of cold-sprayed Ti-6Al-4V at the micro- and nano-scale. *J. Therm. Spray Technol.* **2015**, *24*, 1277–1288. [CrossRef]
49. Li, W.Y.; Zhang, C.; Guo, X.; Xu, J.; Li, C.J.; Liao, H.; Coddet, C.; Khor, K.A. Ti and Ti-6Al-4V coatings by cold spraying and microstructure modification by heat treatment. *Adv. Eng. Mater.* **2007**, *9*, 418–423. [CrossRef]
50. Aydin, H.; Alomair, M.; Wong, W.; Vo, P.; Yue, S. Cold sprayability of mixed commercial purity Ti plus Ti6Al4V metal powders. *J. Therm. Spray Technol.* **2017**, *26*, 360–370. [CrossRef]
51. Garrido, M.A.; Sirvent, P.; Poza, P. Evaluation of mechanical properties of Ti6Al4V cold sprayed coatings. *Sur. Eng.* **2018**, *34*, 399–406. [CrossRef]
52. *ASTM B822-10 Standard Test Method for Particle Size Distribution of Metal Powders and Related Compounds by Light Scattering*; ASTM International: West Conshohocken, PA, USA, 2010.
53. Tan, A.W.Y.; Sun, W.; Phang, Y.P.; Dai, M.; Marinescu, I.; Dong, Z.; Liu, E. Effects of traverse scanning speed of spray nozzle on the microstructure and mechanical properties of cold-sprayed Ti6Al4V coatings. *J. Therm. Spray Technol.* **2017**, *26*, 1484–1497. [CrossRef]
54. Kinetic Spray Solutions. Available online: https://kinetic-spray-solutions.com/ (accessed on 19 January 2018).
55. Coddet, P.; Verdy, C.; Coddet, C.; Debray, F. Effect of cold work, second phase precipitation and heat treatments on the mechanical properties of copper-silver alloys manufactured by cold spray. *Mater. Sci. Eng. A* **2015**, *637*, 40–47. [CrossRef]
56. *ASTM C633-13 Standard Test Method for Adhesion or Cohesion Strength of Thermal Spray Coatings*; ASTM International: West Conshohocken, PA, USA, 2013.
57. Rahmati, S.; Ghaei, A. The use of particle/substrate material models in simulation of cold-gas dynamic-spray process. *J. Therm. Spray Technol.* **2014**, *23*, 530–540. [CrossRef]
58. Hassani-Gangaraj, M.; Veysset, D.; Champagne, V.K.; Nelson, K.A.; Schuh, C.A. Adiabatic shear instability is not necessary for adhesion in cold spray. *Acta Mater.* **2018**, *158*, 430–439. [CrossRef]
59. Bae, G.; Jang, J.I.; Lee, C. Correlation of particle impact conditions with bonding, nanocrystal formation and mechanical properties in kinetic sprayed nickel. *Acta Mater.* **2012**, *60*, 3524–3535. [CrossRef]
60. Song, X.; Everaerts, J.; Zhai, W.; Zheng, H.; Tan, A.W.Y.; Sun, W.; Li, F.; Marinescu, I.; Liu, E.; Korsunsky, A.M. Residual stresses in single particle splat of metal cold spray process – Numerical simulation and direct measurement. *Mater. Lett.* **2018**, *230*, 152–156. [CrossRef]
61. Lek, J.Y.; Bhowmik, A.; Tan, A.W.-Y.; Sun, W.; Song, X.; Zhai, W.; Buenconsejo, P.J.; Li, F.; Liu, E.; Lam, Y.M.; et al. Understanding the microstructural evolution of cold sprayed Ti-6Al-4V coatings on Ti-6Al-4V substrates. *Appl. Surf. Sci.* **2018**, *459*, 492–504. [CrossRef]
62. Guetta, S.; Berger, M.H.; Borit, F.; Guipont, V.; Jeandin, M.; Boustie, M.; Ichikawa, Y.; Sakaguchi, K.; Ogawa, K. Influence of particle velocity on adhesion of cold-sprayed splats. *J. Therm. Spray Technol.* **2009**, *18*, 331–342. [CrossRef]
63. Saleh, M.; Luzin, V.; Spencer, K. Analysis of the residual stress and bonding mechanism in the cold spray technique using experimental and numerical methods. *Surf. Coat. Technol.* **2014**, *252*, 15–28. [CrossRef]
64. Zhu, L.; Jen, T.-C.; Pan, Y.-T.; Chen, H.-S. Particle bonding mechanism in cold gas dynamic spray: A three-dimensional approach. *J. Therm. Spray Technol.* **2017**, *26*, 1859–1873. [CrossRef]
65. Xie, W.; Alizadeh-Dehkharghani, A.; Chen, Q.; Champagne, V.K.; Wang, X.; Nardi, A.T.; Kooi, S.; Muftu, S.; Lee, J.H. Dynamics and extreme plasticity of metallic microparticles in supersonic collisions. *Sci. Rep.* **2017**, *7*, 5073. [CrossRef] [PubMed]

66. Meng, F.; Yue, S.; Song, J. Quantitative prediction of critical velocity and deposition efficiency in cold-spray: A finite-element study. *Scr. Mater.* **2015**, *107*, 83–87. [CrossRef]
67. Li, W.Y.; Zhang, C.; Li, C.J.; Liao, H. Modeling aspects of high velocity impact of particles in cold spraying by explicit finite element analysis. *J. Therm. Spray Technol.* **2009**, *18*, 921. [CrossRef]
68. Ghelichi, R.; Bagherifard, S.; Guagliano, M.; Verani, M. Numerical simulation of cold spray coating. *Surf. Coat. Technol.* **2011**, *205*, 5294–5301. [CrossRef]
69. Brunig, M.; Driemeier, L. Numerical simulation of Taylor impact tests. *Int. J. Plast.* **2007**, *23*, 1979–2003. [CrossRef]
70. Manes, A.; Lumassi, D.; Giudici, L.; Giglio, M. An experimental–numerical investigation on aluminium tubes subjected to ballistic impact with soft core 7.62 ball projectiles. *Thin Walled Struct.* **2013**, *73*, 68–80. [CrossRef]
71. Lesuer, D. *Experimental investigation of material models for Ti-6Al-4V and 2024-T3*; Lawrence Livermore National Laboratory: Livermore, CA, USA, 2000; pp. 1–36.
72. Maev, R.G.; Leshchynsky, V. *Cold gas dynamic spray*, 1st ed.; CRC Press: Boca Raton, FL, USA, 2016.
73. Alkhimov, A.P.; Kosarev, V.F.; Klinkov, S.V. The features of cold spray nozzle design. *J. Therm. Spray Technol.* **2001**, *10*, 375–381. [CrossRef]
74. Haynes, W.M. *Handbook of Chemistry and Physics*, 92nd ed.; CRC Press: Boca Raton, FL, USA, 2011.
75. *Mineral Commodity Summaries 2012*; U.S. Geological Survey: Reston, VA, USA, 2012.
76. Blose, R.E.; Walker, B.H.; Walker, R.M.; Froes, S.H. New opportunities to use cold spray process for applying additive features to titanium alloys. *Met. Powder Rep.* **2006**, *61*, 30–37. [CrossRef]
77. Khun, N.W.; Tan, A.W.Y.; Sun, W.; Liu, E. Wear and corrosion resistance of thick Ti-6Al-4V coating deposited on Ti-6Al-4V substrate via high-pressure cold spray. *J. Therm. Spray Technol.* **2017**, *26*, 1393–1407. [CrossRef]
78. Tan, A.W.Y.; Sun, W.; Khun, N.W.; Marinescu, I.; Dong, Z.; Liu, E. Potential of cold spray as additive manufacturing for Ti6Al4V. In Proceedings of the 2nd International Conference on Progress in Additive Manufacturing (Pro-AM 2016), Nanyang, Singapore, 16–19 May 2016; pp. 403–408.
79. Jung, H.B.; Park, J.I.; Park, S.H.; Kim, H.-J.; Lee, C.-h.; Han, J.-W. Effect of the expansion ratio and length ratio on a gas-particle flow in a converging-diverging cold spray nozzle. *Met. Mater. Int.* **2009**, *15*, 967–970. [CrossRef]
80. Morgan, R.; Fox, P.; Pattison, J.; Sutcliffe, C.; O'Neill, W. Analysis of cold gas dynamically sprayed aluminium deposits. *Mater. Lett.* **2004**, *58*, 1317–1320. [CrossRef]
81. Goldbaum, D.; Chromik, R.R.; Brodusch, N.; Gauvin, R. Microstructure and mechanical properties of Ti cold-spray splats determined by electron channeling contrast imaging and nanoindentation mapping. *Microsc. Microanal.* **2015**, *21*, 570–581. [CrossRef] [PubMed]
82. Wang, K.Y.; Shen, T.D.; Quan, M.X.; Wei, W.D. Hall-Petch relationship in nanocrystalline titanium produced by ball-milling. *J. Mater. Sci. Lett.* **1993**, *12*, 1818–1820. [CrossRef]
83. Pawlowski, L. Chapter 8: Properties of coatings. In *The Science and Engineering of Thermal Spray Coatings*, 2nd ed.; John Wiley & Sons: Chichester, UK, 2008.
84. Tan, A.W.-Y.; Sun, W.; Bhowmik, A.; Lek, J.Y.; Marinescu, I.; Li, F.; Khun, N.W.; Dong, Z.; Liu, E. Effect of coating thickness on microstructure, mechanical properties and fracture behaviour of cold sprayed Ti6Al4V coatings on Ti6Al4V substrates. *Surf. Coat. Technol.* **2018**, *349*, 303–317. [CrossRef]
85. Dodd, B.; Bai, Y. *Adiabatic shear localization: Frontiers and Advances*, 2nd ed.; Elsevier: London, UK, 2012.
86. Huang, R.; Ma, W.; Fukanuma, H. Development of ultra-strong adhesive strength coatings using cold spray. *Surf. Coat. Technol.* **2014**, *258*, 832–841. [CrossRef]